The impact of anion mixing on Li+ coordination and transport properties in pyrrolidinium-based ionic liquid electrolytes

Citation for the original published paper (version of record):
Abdou, N., Wu, Q., Evenäs, L. et al (2026). The impact of anion mixing on Li+ coordination and transport properties in pyrrolidinium-based
ionic liquid electrolytes. Physical Chemistry Chemical Physics, 28(20): 12508-12516.
http://dx.doi.org/10.1039/D6CP00353B

(article starts on next page)

PCCP

PAPER

Cite this: *Phys. Chem. Chem. Phys.*, 2026, **28**, 12508

The impact of anion mixing on Li^+ coordination and transport properties in pyrrolidinium-based ionic liquid electrolytes

Nicole Abdou, †*[a] Quan Wu,†[b] Lars Evenäs, [a] Anna Martinelli [a] and Aleksandar Matic *[b]

Received 30th January 2026,
Accepted 22nd April 2026

DOI: 10.1039/d6cp00353b

rsc.li/pccp

A series of pyrrolidinium-based ionic liquid electrolytes were investigated to explore the potential benefits of incorporating mixed anions, such as bis(fluorosulfonyl)imide and bis(trifluoromethylsulfonyl)-imide used in this study. The effect of mixing anions on fundamental physicochemical properties was investigated, with particular emphasis on transport properties and lithium-ion coordination. More specifically, the electrolytes were systematically characterized in terms of phase behavior, density, viscosity, transport properties (ionic conductivity and self-diffusion), and intermolecular interactions. The results show that mixing anions modifies the nature of intermolecular interactions, which, in turn, alters the coordination of Li^+ with its counterions. In the case of the $(LiFSI)_{0.2}(Pyr_{14}TFSI)_{0.8}$ sample, this resulted in improved thermal and transport properties, anticipating an improved performance in lithium-ion batteries.

1 Introduction

Ionic liquids (ILs) are a unique class of compounds that consist of (ideally) only ions and have a melting point below 100 °C.[1] Notably, by selecting a specific combination of anions and cations, the physico-chemical properties of an ionic liquid can be tuned to suit specific applications.[2] Furthermore, compared to conventional solvents, ILs exhibit broader electrochemical stability windows, good ionic conductivity, high thermal stability, non-flammability and low volatility. Consequently, they have been extensively studied for various applications, such as catalysis,[3] gas separation,[4–6] and energy storage devices, including lithium-ion batteries.[7–9]

Among the vast variety of ionic liquids, those based on pyrrolidinium have been extensively studied for lithium-ion batteries due to their capacity to support lithium electrochemistry and promote the formation of a stable solid electrolyte interphase (SEI).[10,11] However, a key challenge in using ionic liquids in Li-ion batteries is their limited transport properties (*i.e.*, slow Li^+ transport) and strong Li^+–anion interactions. Several strategies have been considered to address this issue, mainly aiming to enhance the diffusivity of the lithium ions. These include the use of molecular additives,[12] eutectic mixtures,[13,14] and binary/ternary ionic liquid systems.[15–19] Appetecchi *et al.* investigated a mixture of *N*-methyl-*N*-propyl pyrrolidinium bis(fluorosulfonyl)imide ($Pyr_{13}FSI$) and *N*-butyl-*N*-propyl pyrrolidinium bis(trifluoromethanesulfonyl)imide ($Pyr_{14}TFSI$) ILs with 0.3 M of either lithium hexafluorophosphate ($LiPF_6$) or lithium bis(trifluoromethanesulfonyl)imide (LiTFSI) salts. Their findings demonstrated enhanced ionic conductivity in ternary systems compared to binary ones, with a stronger effect at low temperatures.[20] Zhou *et al.* examined the phase behavior of the same systems, reporting the absence of phase transitions beyond a molar ratio of 0.3 with either salt.[21,22] Moreover, Bayley *et al.* studied ternary systems having Pyr_{13} as the common cation, paired with either FSI or TFSI anions over a broad compositional range in the presence of a lithium salt (0.5 m). Their results showed increased diffusivity of Li and TFSI ions upon addition of FSI.[23] Nádherná *et al.* investigated the electrochemical performance, in Li-ion batteries, of binary systems containing 0.7 M LiFSI or LiTFSI in $Pyr_{14}TFSI$. The authors reported higher charge/discharge capacities and improved electrochemical stability in the LiFSI/$Pyr_{14}TFSI$ mixed anion system.[24] Similarly, Lahiri *et al.* observed comparable results in a 1 M LiTFSI/$Pyr_{14}FSI$ system.[25]

To strengthen the understanding of the molecular interactions and transport mechanisms in these mixed-anion ionic liquid electrolytes, a multi-technique approach was employed to investigate mixtures of Pyr_{14}-based ionic liquids and lithium salts. An in-depth analysis of their phase behavior, transport

---

[a] *Department of Chemistry and Chemical Engineering, Chalmers University of Technology, SE-412 96 Gothenburg, Sweden. E-mail: nicole.abdou@chalmers.se*
[b] *Department of Physics, Chalmers University of Technology, SE-412 96 Gothenburg, Sweden. E-mail: matic@chalmers.se*

† These authors contributed equally to this work.

properties, Li-ion coordination and intermolecular interactions was conducted, providing a side-by-side explanation of how Li^+ mobility is related to Li-ion coordination.

2 Experimental details

2.1 Chemicals

The lithium bis(trifluoromethylsulfonyl)imide (LiTFSI) (99.9%) and lithium bis(fluorosulfonyl)imide (LiFSI) (99.9%) salts, along with 1-butyl-1-methylpyrrolidinium bis(fluorosulfonyl)imide ($Pyr_{14}FSI$) (99.9%) and 1-butyl-1-methylpyrrolidinium bis(trifluoromethylsulfonyl)imide ($Pyr_{14}TFSI$) (99.9%) ionic liquids, were purchased from Solvionic. The molecular structures of the ions found in the ionic liquids and in the salts are shown in Fig. 1. All compounds were dried under vacuum in a Büchi oven at 353 K for 12 hours and then stored in an argon-filled glovebox, before mixing and investigations.

2.2 Preparation

Samples were prepared by mixing ionic liquids and Li salts in a $0.2LiA_1 : 0.8Pyr_{14}A_2$ molar ratio, where A_1 and A_2 represent the FSI or the TFSI anion. All samples were prepared and stored in an argon-filled glovebox with O_2 and H_2O levels below 1 ppm. Throughout the following text, the samples are named $(LiA_1)_{0.2}(Pyr_{14}A_2)_{0.8}$.

2.3 Methods

2.3.1 Differential scanning calorimetry (DSC). DSC measurements were performed using a DSC 250 from TA Instruments. Samples were placed in hermetic aluminum pans and sealed in an argon-filled glovebox. DSC thermograms were collected under helium flow (50 mL min^{-1}), over the temperature range of 123 K to 373 K with heating and cooling rates of 5 K min^{-1}. Two scans were recorded for each measurement. The glass transition temperatures (T_g) were extracted from the second heating scan curves using sigmoid functions and the identification of the inflection points.

2.3.2 Viscosity and density. Viscosity and density measurements were carried out using an Anton Paar DMA 4500 M oscillation U-tube densitometer over the temperature range of 293 K to 353 K in 10 K increments. The density accuracy is about ±0.0001 g cm^{-3}. The viscosity was determined using a Lovis 2000 ME rolling ball viscometer module, using which the dynamic viscosity (μ) was estimated from the density of the fluid (ρ) and the velocity of the falling ball (ν), as $\mu = \rho \cdot \nu$. The viscosity measurement has an accuracy of up to 0.1% and a repeatability of 0.5%. The temperature accuracy is ±0.02 K with a repeatability of ±0.005 K.

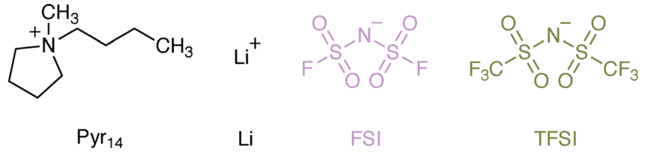

Fig. 1 Molecular structure of the 1-butyl-1-methylpyrrolidinium (Pyr_{14}) and lithium (Li) cations and the bis(fluorosulfonyl)imide (FSI) and the bis(trifluoromethylsulfonyl)imide (TFSI) anions.

2.3.3 Dielectric spectroscopy. Conductivity data were collected using a novocontrol GmBH broadband dielectric spectrometer, a parallel plate sample cell with stainless steel electrodes and a 3 mm spacer. Measurements were conducted in the frequency range of 10^{-2}–10^7 Hz and the temperature range of 173–373 K. Data were collected every 10 K with a stabilization time of 180 s at each temperature. From three repeated measurements of the same solution, a value for the standard deviation has been estimated.

2.3.4 Nuclear magnetic resonance diffusometry. NMR experiments were performed using an AVANCE III HD Bruker NMR spectrometer, operating at 14.1 T and equipped with a Diff30 probe connected to a 60 A gradient amplifier. RF coil inserts of a 5 mm $^1H/^2H$ double coil, a 5 mm ^{19}F single coil, and a 5 mm ^7Li single coil configuration were used. The self-diffusion coefficients of the different species, *i.e.*, Pyr_{14} (^1H), FSI/TFSI (^{19}F) and Li cation (^7Li), were determined at five different temperatures in the range of 298–353 K. A 5 mm NMR tube was filled (∼1.5 cm) with the liquid sample and sealed in the glovebox using PTFE sealing tape. A regular stimulated echo NMR sequence (diffste) was used at room temperature. However, a double stimulated echo NMR sequence (diffDste) was employed at higher temperatures to ensure that thermal convection did not affect the results. An 18 μs 90-degree pulse, a 2 s acquisition time, a 5 s recycling delay, a 100 ms diffusion delay (Δ) and a 1 ms gradient pulse duration (δ) were used. The maximum gradient strength (g) varied in the range of 100–1200 Gauss per cm while keeping k constant; k is defined as

$$k = (\delta \cdot \gamma \cdot g)^2(\Delta - \delta/3) \quad (1)$$

where Δ is the diffusion delay time, δ is the gradient pulse duration, γ is the gyromagnetic ratio of the studied nucleus and g is the gradient strength.

The gradient strengths were calibrated using reference samples with known self-diffusion coefficients; the ^1HDO trace signals in the D_2O reference sample, hexafluorobenzene (C_6F_6) and a standard 1 M LiCl in the H_2O sample were recorded for ^1H, ^{19}F and ^7Li, respectively.[26] To determine the intensity attenuation, the average of all ^1H NMR signals was considered for the Pyr_{14} cation. For the Li cation, the signal at −0.4 ppm in the ^7Li spectrum was utilized, while the signals at −80 ppm and 50 ppm in the ^{19}F spectrum were used for the TFSI and FSI anions, respectively.

2.3.5 Raman spectroscopy. Raman spectra were recorded using a Bruker MultiRAM Fourier transform Raman spectrometer equipped with a Nd:YAG laser (1064 nm) and a liquid nitrogen-cooled Ge diode detector. The nominal laser power was set to 720 mW, with a spectral resolution of 2 cm^{-1} (full width at half-maximum). A Blackman–Harris three-term window function was applied for apodization, and the spectra were acquired as the average of 1000 scans. In order to estimate the integrated areas under selected peaks, a multi-peak fitting procedure based on a linear background and Voigt profiles was applied using the Origin lab software. The spectral region 680–780 cm^{-1} was deconvoluted into six contributions, corresponding to spectroscopically free FSI (I, separated from cations), weakly coordinated FSI (II, contact ion pairs), strongly coordinated FSI–Li$^+$ (III, ion aggregates), the two conformers (cisoid (IV) and transoid (V)) of spectroscopically free TFSI, and coordinated TFSI–Li$^+$ (VI). In the fitting procedure, peak positions, full widths at half maximum (FWHM), and Voigt profiles were fixed, while heights were left as a free fit parameter. The population of the "free" and "coordinated" anions was estimated from the relative intensities of the six components, as expressed below:

$$C_{\text{free FSI}} = \frac{A_{\text{I}}}{A_{\text{I}} + A_{\text{II}} + A_{\text{III}}} \tag{2}$$

$$C_{\text{coordinated FSI}} = \frac{A_{\text{II}} + A_{\text{III}}}{A_{\text{I}} + A_{\text{II}} + A_{\text{III}}} \tag{3}$$

$$C_{\text{free TFSI}} = \frac{A_{\text{IV}} + A_{\text{V}}}{A_{\text{IV}} + A_{\text{V}} + A_{\text{VI}}} \tag{4}$$

$$C_{\text{coordinated TFSI}} = \frac{A_{\text{VI}}}{A_{\text{IV}} + A_{\text{V}} + A_{\text{VI}}} \tag{5}$$

where A_{I}, A_{II}, A_{III}, A_{IV}, A_{V}, and A_{VI} are the integrated areas of contributions I, II, III, IV, V and VI, respectively. These calculations are valid assuming that the Raman activities of the different TFSI and FSI conformations are equivalent,[27,28] so the integrated areas directly reflect their relative populations. Then, the average number of FSI and TFSI anions coordinating with Li$^+$ ($N_{\text{anion–Li}^+}$) was determined using the following equation:

$$N_{\text{anion}-\text{Li}^+} = \frac{C_{\text{coordinated anion}}}{x} \tag{6}$$

where x is the molar fraction of Li$^+$ ions.

3 Results and discussion

For a comprehensive understanding of the transport properties of the electrolytes at focus in this work, their phase behavior, viscosity, density, ionic conductivity and self-diffusion, as well as intermolecular interactions, with a focus on coordination, were investigated.

3.1 Phase behavior

The phase behavior was investigated using DSC, and the DSC thermograms are shown in Fig. 2. Both neat ionic liquids, Pyr$_{14}$FSI and Pyr$_{14}$TFSI, show melting peaks and glass transition from which the glass transition temperature (T_g) was determined. The T_g of Pyr$_{14}$FSI is found around 165 K, while that of Pyr$_{14}$TFSI is slightly higher, observed at about 184 K.[29] In addition, the DSC curves of the neat ionic liquids reveal cold crystallization and solid–solid transitions. However, the phase behavior is significantly altered with the addition of Li salts. Either salt in the Pyr$_{14}$FSI-based systems inhibits recrystallization and stabilizes the liquid phase down to the T_g, which is found at 175 K. For Pyr$_{14}$TFSI with added LiTFSI, recrystallization and melting are still observed; however, these transitions are suppressed upon mixing anions, *i.e.*, with the addition of LiFSI. Interestingly, the glass transition temperature increases by 11 K when LiTFSI is added to Pyr$_{14}$TFSI, whereas a T_g similar to that of the neat IL is observed for the mixed-anion system (LiFSI added to Pyr$_{14}$TFSI), see also the values in Table 1. Thus, the incorporation of LiFSI into a TFSI-based ionic liquid has a more pronounced effect compared to the reversed scenario. Interestingly, an opposite trend was observed for imidazolium-based electrolytes.[30]

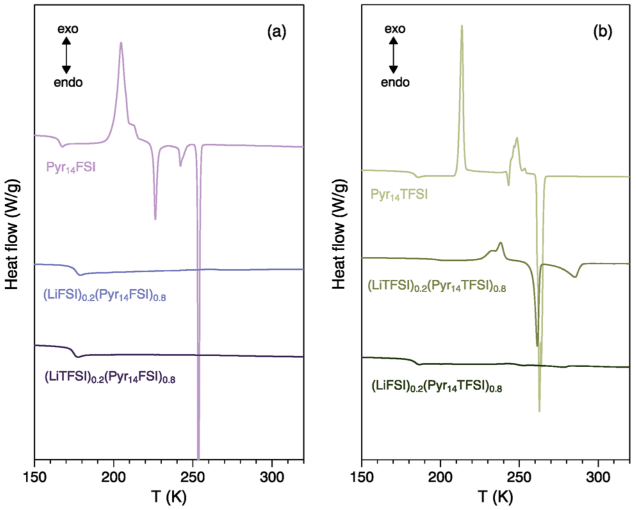

Fig. 2 DSC thermograms of Pyr$_{14}$FSI (a) and Pyr$_{14}$TFSI (b) based samples.

Table 1 Glass transition temperatures (T_g) of all ionic liquid electrolytes, extracted from the second heating scan of the DSC curve

Sample	T_g (K)
Pyr$_{14}$FSI	165
(LiFSI)$_{0.2}$(Pyr$_{14}$FSI)$_{0.8}$	175
(LiTFSI)$_{0.2}$(Pyr$_{14}$FSI)$_{0.8}$	175
Pyr$_{14}$TFSI	184
(LiTFSI)$_{0.2}$(Pyr$_{14}$TFSI)$_{0.8}$	195
(LiFSI)$_{0.2}$(Pyr$_{14}$TFSI)$_{0.8}$	184

3.2 Viscosity and density

Viscosity and density values, measured as a function of temperature, are shown in Fig. 3a and b. Corresponding values are summarized in Table S1. In Pyr$_{14}$FSI-based electrolytes, the addition of either lithium salt leads to an increase in both density and viscosity. For the electrolytes based on Pyr$_{14}$TFSI, the addition of LiTFSI salt leads to an increase in density and viscosity compared to the neat ionic liquid, whereas, upon the addition of LiFSI, these increases are less pronounced, resulting in lower density and viscosity compared to those of the LiTFSI-containing electrolytes. Overall, Pyr$_{14}$FSI-based electrolytes exhibit lower viscosity and density compared to the Pyr$_{14}$TFSI-based electrolytes, as previously reported in the literature.[31] These results suggest that anion mixing in

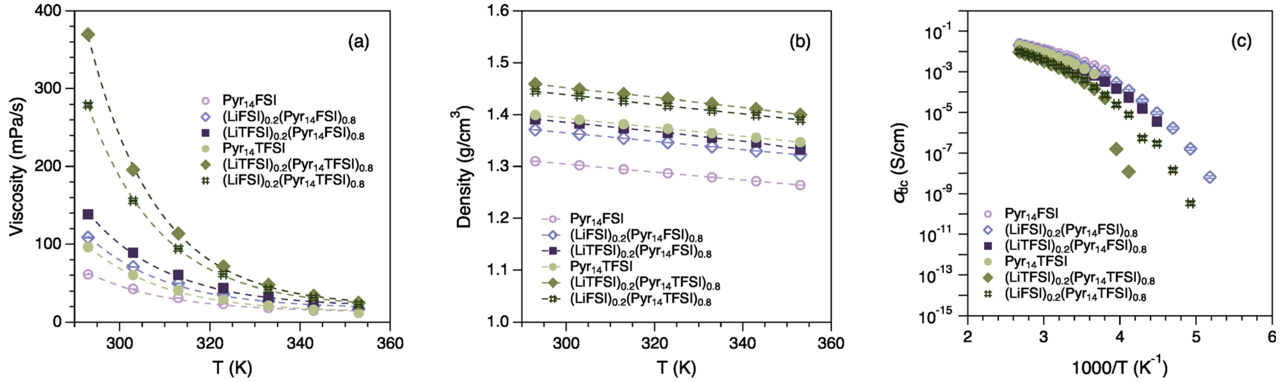

Fig. 3 Viscosity (a), density (b) and ionic conductivity (c) values measured as a function of temperature. The dashed lines are guides to the eyes. The error bars are smaller than the plotted symbols and are therefore not visible.

$Pyr_{14}TFSI$-based electrolytes significantly modifies the intermolecular interactions, with possible effects on the Li^+–anion coordination.

3.3 Transport properties

The ionic conductivity was measured in the temperature range 193–373 K, using a broadband dielectric spectrometer (BDS), and the measured values are plotted in Fig. 3c. The ionic conductivity values are summarized in Table S2. For all electrolytes, the ionic conductivity increases with increasing temperature. The neat $Pyr_{14}FSI$ exhibits higher ionic conductivity than $Pyr_{14}TFSI$, in agreement with the viscosity trend above and with the literature.[31] In general, the addition of a Li salt to the neat ionic liquids leads to a decrease in ionic conductivity, which can be attributed to the corresponding increase in viscosity discussed above.

The measured density, viscosity and conductivity data were used to create a Walden plot with the aim of highlighting differences in ionic association and related transport mechanisms. The Walden plot is generally based on the Walden equation described by Angell *et al.*:[32]

$$\Lambda \cdot \eta^{\alpha} = C \tag{7}$$

where Λ is the molar conductivity, η is the viscosity, α is an adjustable parameter and C is a temperature dependent constant.

The Walden plots of all electrolytes are shown in Fig. 4. In this plot, the diagonal line represents the behavior expected from an aqueous solution of 0.01 M KCl, in which all ions are assumed to be dissociated and to diffuse independent of each other. A negative deviation from the reference line, also known as the ideal line, can be seen as a measure of ion association within the ionic liquid system, a rationale for the conductivity being lower than expected from the mobility of free ions.[32] The data of all investigated ionic liquids fall below the ideal line, with deviations ranging from −0.140 to −0.343, increasing from the neat ionic liquids to the electrolytes (Table S3). This implies, according to Angell *et al.*, the presence of ionic interactions that prevent full ion dissociation.[32] Additionally, upon the addition of a salt, the Walden plots of the $Pyr_{14}TFSI$-based ionic liquids show a slightly greater deviation from the ideal line than those of $Pyr_{14}FSI$-based ionic liquids. The slopes of all lines, reflecting the temperature dependence of ion association, are approximately 0.90, consistent with values typically reported for ionic liquids.[32–35]

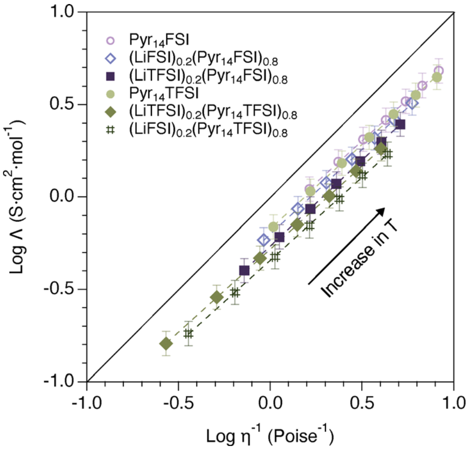

Fig. 4 Walden plot for $Pyr_{14}FSI$ and $Pyr_{14}TFSI$ based samples.

The ionic conductivity values of the mixed-anion electrolytes were also plotted on a T_g-scaled Arrhenius plot (an Angell's plot), normalizing the temperature scale to each material's glass transition temperature, Fig. 5. The T_g values used in this approach are those obtained from the DSC data discussed above, also reported in Fig. 1. This representation allows extending the discussion of ionic conductivity to the concept of fragility; fragility is a fundamental property of glass-forming liquids that describes how rapidly the dynamics change upon heating from the glass transition temperature T_g, or *vice versa*. In an Angell's plot, fragile liquids display a strong curvature, whereas stronger liquids exhibit a closer to linear behavior. In Fig. 5, the ionic conductivity values for the two samples converge onto a single curve, revealing similar fragility and indicating that their temperature-dependent conductivities evolve in a comparable manner relative to T_g, despite differences in composition and glass transition temperatures. Consequently, their dynamics change at a similar rate near T_g, where rapid changes

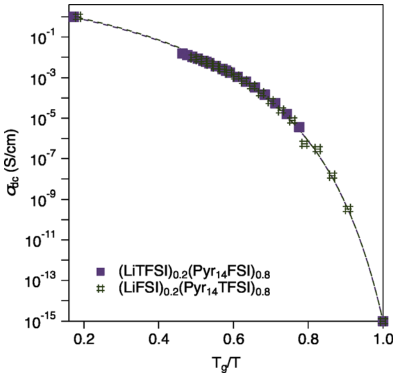

Fig. 5 T_g-scaled plot (Angell plot) of the ionic conductivity of $(LiTFSI)_{0.2}$-$(Pyr_{14}FSI)_{0.8}$ and $(LiFSI)_{0.2}(Pyr_{14}TFSI)_{0.8}$. The dashed lines are guides to the eyes. The error bars are smaller than the plotted symbols and are therefore not visible.

in dynamics facilitate higher mobilities at elevated temperatures, an advantageous behavior for practical applications.[36]

To selectively distinguish Li^+ ion transport, which cannot be resolved by BDS, the self-diffusion coefficients of all involved ionic species, *i.e.*, Pyr_{14}, Li^+, FSI and TFSI, were estimated using NMR diffusometry, Fig. 6a–f. The extracted self-diffusion coefficient values are summarized in Table S4. While for $Pyr_{14}FSI$, the anion exhibits higher diffusivity than the cation, the opposite trend is observed for $Pyr_{14}TFSI$. This finding aligns with earlier studies and may be attributed to the size difference between the FSI and TFSI anions.[37–40] When salts are added, the self-diffusion coefficients of all ions decrease due to increased viscosity, in agreement with the viscosity and conductivity data discussed above. Interestingly, the addition of LiFSI to $Pyr_{14}TFSI$ leads to a smaller decrease in diffusion coefficient than the addition of LiTFSI (especially at lower temperatures). This difference may be attributed to the smaller size of the FSI anion, favoring fluidity. Importantly, in FSI-based systems, the self-diffusion coefficients of all ions, including the Li^+, remain higher than those of TFSI-based systems, consistent with previously reported results.[15,39] The relative contribution of Li^+ ions to the overall conductivity can be estimated by calculating the apparent transference number (t_{Li^+}) from the diffusion data. High Li^+ transference numbers are essential for efficient charge–discharge performance in Li-ion batteries. Across all studied electrolytes, the t_{Li^+} remains approximately 0.07 with a negligible temperature dependence (Table S5). These values are consistent with the literature and indicate that the Li^+ contribution to the conductivity remains similar across all four electrolytes.

To gain deeper insight into the degree of ion dissociation, the ratio of molar conductivity Λ/Λ_{NE}, also known as ionicity,

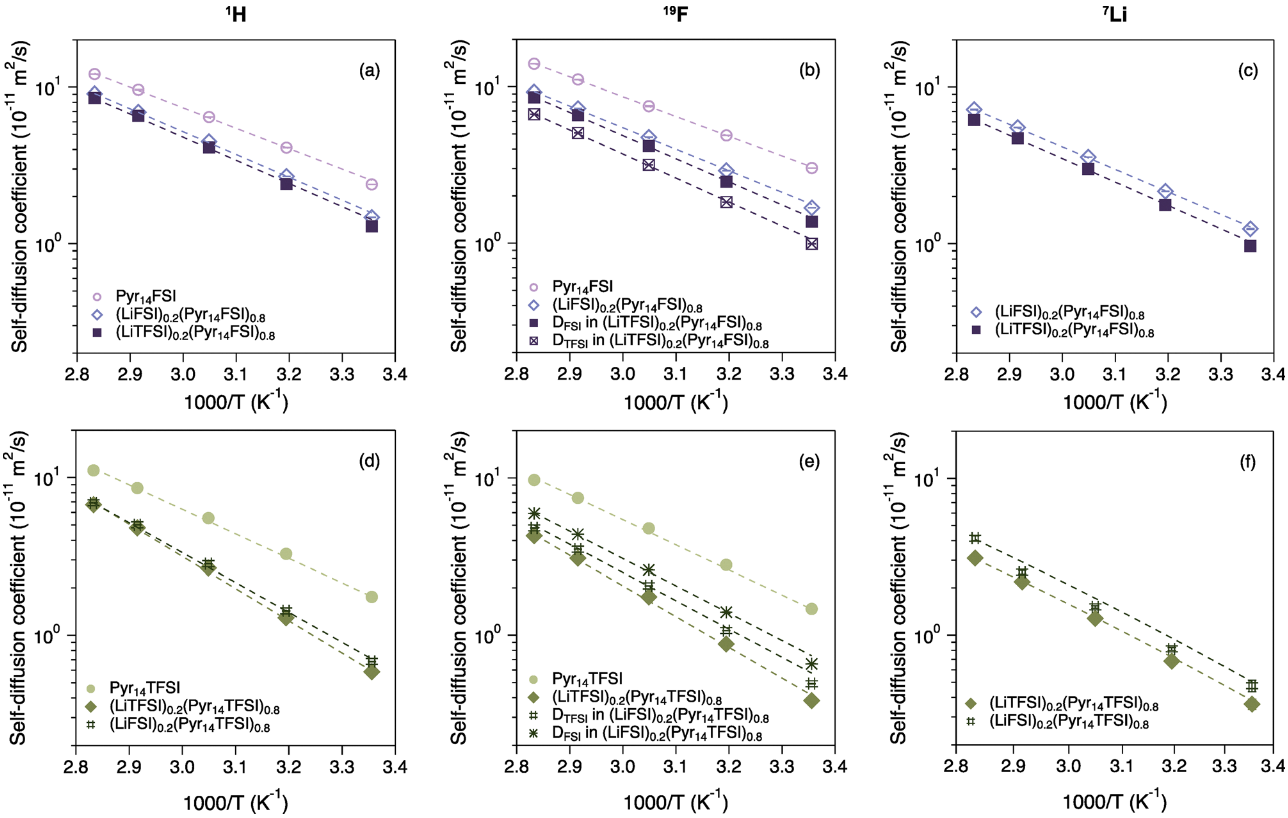

Fig. 6 The three upper panels and the three bottom panels show the self-diffusion coefficients estimated for the $Pyr_{14}FSI$ based (a)–(c) and the $Pyr_{14}TFSI$ based (d)–(f) samples, respectively. The first (a) and (d), second (b) and (e) and third (c) and (f) columns show self-diffusion values measured from the ^1H, ^{19}F and ^7Li nuclei. Dashed lines are guides to the eyes. The error bars are smaller than the plotted symbols and are therefore not visible.

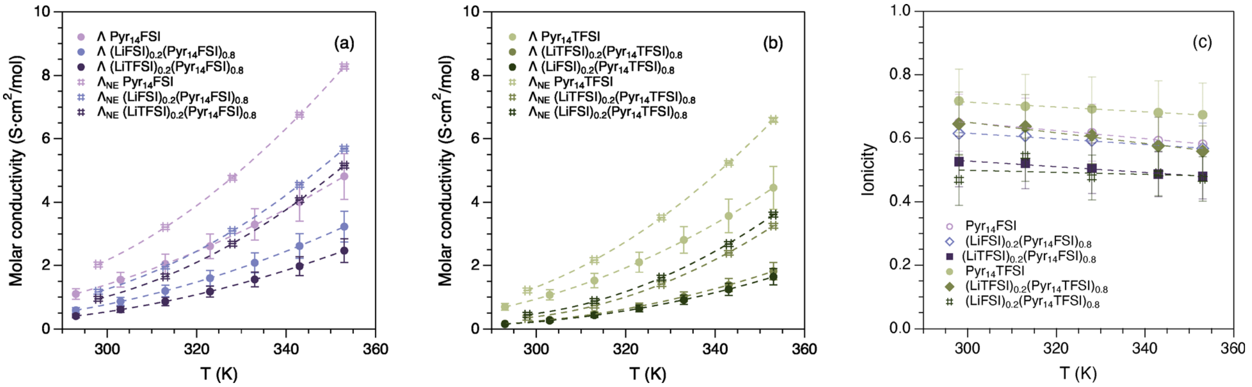

Fig. 7 Molar conductivities obtained from NMR and impedance measurements for $Pyr_{14}FSI$ (a) and $Pyr_{14}TFSI$ (b) based samples. Estimated ionicity values as a function of temperature (c).

was estimated.[41–43] Λ is the molar conductivity obtained from impedance measurements (eqn (8)), while Λ_{NE} is the molar conductivity calculated from the self-diffusion coefficients using the Nernst–Einstein equation (eqn (9)):

$$\Lambda = \frac{\sigma_{dc} \cdot M_{sol}}{\rho} \tag{8}$$

with σ_{dc} being the ionic conductivity measured by BDS, M_{sol} the molar mass of the solution = $\chi_{IL} \cdot M_{IL}$ + $\chi_{salt} \cdot M_{salt}$ and ρ the density of the solution,

$$\Lambda_{NE} = \frac{\left(x_{Pyr_{14}} \cdot D_{Pyr_{14}} + x_{TFSI} \cdot D_{TFSI} + x_{FSI} \cdot D_{FSI} + x_{Li^+} \cdot D_{Li^+}\right) \cdot F^2}{R \cdot T} \tag{9}$$

where F is the Faraday constant, R is the universal gas constant and x_i is the molar ratio of the ith component. The molar conductivities and ionicity values are summarized in Table S6. Fig. 7a and b show that Λ is smaller than Λ_{NE} in all systems and at all temperatures. Consequently, the ionicity Λ/Λ_{NE} shows a value ≤ 1 in all studied liquids, as shown in Fig. 7c, indicating that some ionic species diffuse in pairs or clusters, hence not contributing to the macroscopically measured ionic conductivity, in line with the trend observed in the Walden plot (Fig. 4). The ionicity decreases in both systems with the addition of Li salt, in particular, when anions are mixed, highlighting overall stronger interactions and aggregate formation in the electrolytes.

3.4 Ion coordination

Further insight into the nature of intermolecular interactions can be obtained by Raman spectroscopy. Room temperature Raman spectra were recorded for both the neat ionic liquids and the electrolytes, Fig. 8. In $Pyr_{14}TFSI$-based systems, the strongest vibrational mode occurs around 743 cm^{-1}, corresponding to the expansion-contraction mode of the TFSI anion (ν_s S–N–S and ν_s CF_3).[44] The sensitivity of this mode to the coordination of the anion has been thoroughly investigated using both experimental and theoretical methods.[27,45] In the neat $Pyr_{14}TFSI$, TFSI exhibits two coexisting, weakly coordinated conformers (*cis* and *trans*). The two conformers give rise to two closely spaced bands in the Raman spectrum between 740 and 744 cm^{-1}. With the addition of LiTFSI, a new Raman

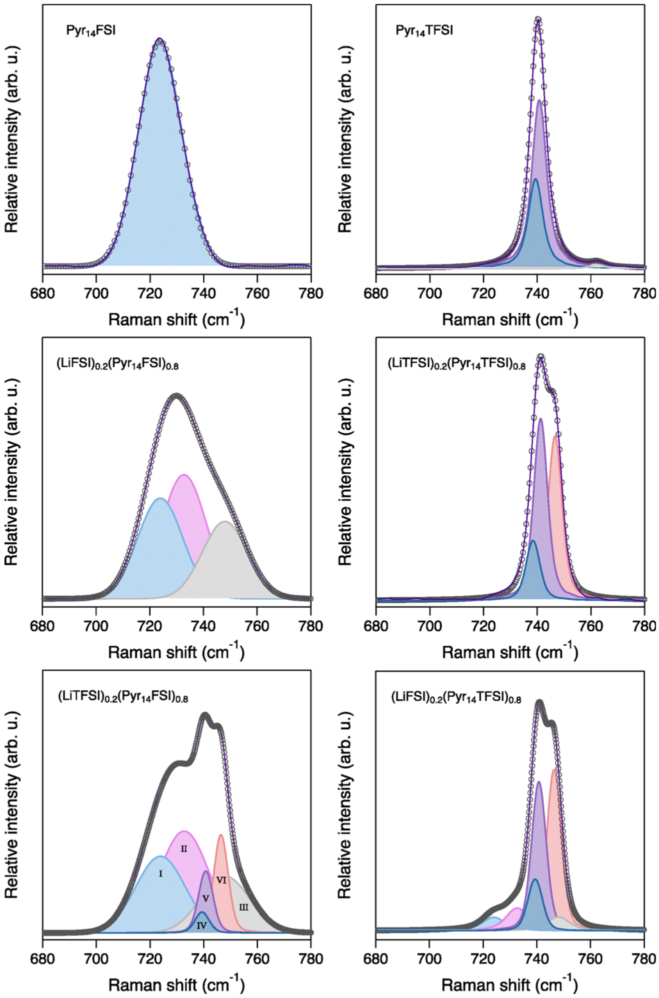

Fig. 8 Experimentally recorded Raman spectra (symbols), fitting peaks (colored Voigt profiles) and fit results (black lines) for all Pyr_{14}-based solutions. Peaks are labeled consistently across all six panels as follows: spectroscopically free FSI (I), weakly coordinated FSI (II), strongly coordinated FSI–Li^+ (III), *cis* (IV) and *trans* (V) conformers of spectroscopically free TFSI, and Li^+-coordinated TFSI (VI).

Table 2 Average number of Li^+-coordinated FSI and TFSI anions ($N_{anion-Li^+}$) estimated from peak fitting the Raman spectra

Samples	N_{FSI-Li^+}	$N_{TFSI-Li^+}$
$(LiTFSI)_{0.2}(Pyr_{14}TFSI)_{0.8}$	—	2.17
$(LiFSI)_{0.2}(Pyr_{14}FSI)_{0.8}$	3.33	—
$(LiFSI)_{0.2}(Pyr_{14}TFSI)_{0.8}$	0.73	1.78
$(LiTFSI)_{0.2}(Pyr_{14}FSI)_{0.8}$	2.70	0.54

band appears at higher frequencies, around 748 cm^{-1}, attributed to TFSI anions coordinating with the Li^+ cation.[46–48] The average number of TFSI anions around a Li^+ anion was calculated to be 2.17 (Table 2).[48] Similarly, FSI in $Pyr_{14}FSI$ exhibits two conformations (C_1 and C_2) that coexist at room temperature, associated with two (theoretically calculated) closely spaced Raman modes at 725 and 732 cm^{-1}. However, a single broader Raman band is typically observed experimentally around 730 cm^{-1}. Upon addition of LiFSI, an additional Raman mode has been reported in the literature at approximately 744 cm^{-1}, corresponding to FSI coordinated with Li^+.[49,50] The calculated average number of FSI anions surrounding Li^+ is 3.33 (Table 2), which is higher than the corresponding number of TFSI in the $(LiTFSI)_{0.2}(Pyr_{14}TFSI)_{0.8}$ sample (2.17). This suggests that Li^+ coordination involves more FSI than TFSI anions, consistent with the results discussed above.

However, mixing anions results in a more complex Li^+ solvation structure. Six Raman modes were identified and fitted, corresponding to two conformers of weakly coordinated TFSI, one Li^+-coordinated TFSI, one free FSI, one weakly coordinated FSI (contact ion pairs) and one strongly FSI coordinated Li^+ (ion aggregates). The calculated average numbers of FSI and TFSI anions coordinating with Li^+ were 0.73 and 1.78 for the $(LiFSI)_{0.2}(Pyr_{14}TFSI)_{0.8}$ sample and 2.70 and 0.54 for the $(LiTFSI)_{0.2}(Pyr_{14}FSI)_{0.8}$ sample. Consequently, the average number of anions around each Li^+ in the $(LiFSI)_{0.2}(Pyr_{14}TFSI)_{0.8}$ sample, with mixed anions, is 2.51 slightly higher than that in the single-anion electrolyte $(LiTFSI)_{0.2}(Pyr_{14}TFSI)_{0.8}$ (2.17). This can be explained by the higher ability of FSI to coordinate with Li^+. In contrast, the average number of anions around Li^+ remains nearly unchanged in the $Pyr_{14}FSI$-based samples.

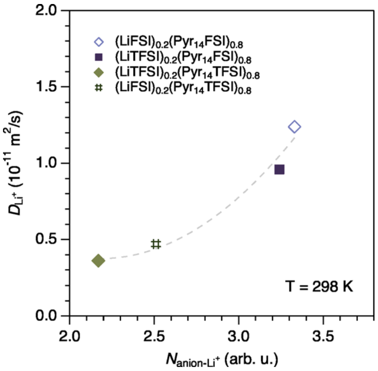

Fig. 9 The Li^+ self-diffusion coefficient (D_{Li^+}) as a function of the average number of Li^+-coordinated anions $N_{anion-Li^+}$). The dashed line is a guide to the eyes.

The total number of anions coordinated with Li ions in the IL system plays a significant role in determining the strength of the Li-ion solvation structure, which, in turn, influences the transport properties of the Li ion. We find that the order of this coordination across the four samples is as follows: $(LiTFSI)_{0.2}(Pyr_{14}TFSI)_{0.8} < (LiFSI)_{0.2}(Pyr_{14}TFSI)_{0.8} < (LiTFSI)_{0.2}(Pyr_{14}FSI)_{0.8} \leq (LiFSI)_{0.2}(Pyr_{14}FSI)_{0.8}$.

These results are consistent with the higher Li^+ self-diffusion coefficients observed for $Pyr_{14}FSI$-based systems compared to their counterparts. Fig. 9 illustrates the correlation between the average number of Li-coordinated anions ($N_{anion-Li^+}$) and Li^+ mobility (D_{Li^+}), showing that an increase in $N_{anion-Li^+}$ is associated with an increase in D_{Li^+}.

Conclusions

In summary, mixtures of pyrrolidinium-based ionic liquids and 0.2 mole fraction of lithium salts with either identical or mixed anions were investigated with a focus on their physicochemical properties, particularly Li-ion diffusion and coordination. The incorporation of lithium salt generally leads to increased viscosity, higher glass transition temperature (T_g), reduced ionic conductivity and slower ion diffusivity compared to those of neat ionic liquid systems. Notably, mixing anions shows a more pronounced effect in $Pyr_{14}TFSI$-based systems, where the addition of FSI anions significantly lowers T_g and enhances both conductivity and ion diffusivity. This behavior is likely due to the smaller size and greater Li-coordinating ability of the FSI anion compared to those of TFSI, which alters the intermolecular interactions within the system. Despite the positive impact of the mixed-anion approach, the larger size of the TFSI anion has a dominant impact reducing ion transport and increasing viscosity, relative to the systems rich in FSI. Although some observed effects, such as the increased viscosity and decreased conductivity, may be expected to persist at other Li salt concentrations, as reported in the literature, further studies are necessary to confirm these trends in the herein studied systems.[30,35] Among the mixed-anion solutions investigated in this work, $(LiTFSI)_{0.2}(Pyr_{14}FSI)_{0.8}$ emerges as a promising candidate for lithium-ion battery electrolytes, due to its favorable balance of transport properties and thermal behavior.

Author contributions

Nicole Abdou: data curation, formal analysis, investigation, methodology, visualization, writing – original draft, and writing – review and editing. Quan Wu: data curation, formal analysis, investigation, methodology, and writing – review and editing. Lars Evenäs: investigation, validation, and writing – review and editing. Anna Martinelli: funding acquisition, supervision, validation, and writing – review and editing. Aleksandar Matic: conceptualization, funding acquisition, resources, supervision, validation, and writing – review and editing.

Conflicts of interest

There are no conflicts to declare.

Data availability

The numerical data used in this manuscript, *i.e.*, values for density, viscosity, ionic conductivity, self-diffusion coefficients, apparent Li^+ transference numbers, molar conductivities, and ionicity are reported in the supplementary information (SI). See DOI: https://doi.org/10.1039/d6cp00353b.

Acknowledgements

Nicole Abdou and Anna Martinelli kindly thank the Areas of Advance *Materials Science* and *Energy* at Chalmers University of Technology for the financial support. Quan Wu and Aleksandar Matic thank the Swedish Electricity Storage and Balancing Centre (SESBC). This project is financed through the Swedish Electricity Storage and Balancing Centre (SESBC). The centre is funded by the Swedish Energy Agency together with five academic and twenty-eight non-academic partners. The authors also thank the Swedish NMR Centre in Gothenburg for the allocated NMR time.

Notes and references

1 Z. Lei, B. Chen, Y.-M. Koo and D. R. MacFarlane, *Chem. Rev.*, 2017, **117**, 6633–6635.
2 M. Freemantle, *Chem. Eng. News Arch.*, 1998, **76**, 32–37.
3 M. Vafaeezadeh and H. Alinezhad, *J. Mol. Liq.*, 2016, **218**, 95–105.
4 Z. Dai, R. D. Noble, D. L. Gin, X. Zhang and L. Deng, *J. Membr. Sci.*, 2016, **497**, 1–20.
5 L. C. Tomé and I. M. Marrucho, *Chem. Soc. Rev.*, 2016, **45**, 2785–2824.
6 I. Harmanli, N. V. Tarakina, M. Antonietti and M. Oschatz, *J. Am. Chem. Soc.*, 2021, **143**, 9377–9384.
7 D. R. MacFarlane, N. Tachikawa, M. Forsyth, J. M. Pringle, P. C. Howlett, G. D. Elliott, J. H. Davis, M. Watanabe, P. Simon and C. A. Angell, *Energy Environ. Sci.*, 2014, **7**, 232–250.
8 M. Watanabe, *Electrochemistry*, 2016, **84**, 642–653.
9 M. Watanabe, M. L. Thomas, S. Zhang, K. Ueno, T. Yasuda and K. Dokko, *Chem. Rev.*, 2017, **117**, 7190–7239.
10 M. Kerner and P. Johansson, *Batteries*, 2018, **4**, 10–22.
11 L. M. McGrath and J. F. Rohan, *Molecules*, 2020, **25**, 6002–6035.
12 F. Lundin, A. Idström, P. Falus, L. Evenäs, S. Xiong and A. Matic, *J. Phys. Chem. C*, 2022, **126**, 16262–16271.
13 P. M. Bayley, A. S. Best, D. R. MacFarlane and M. Forsyth, *Phys. Chem. Chem. Phys.*, 2011, **13**, 4632–4640.
14 M. Middendorf and M. Schonhoff, *J. Phys. Chem. B*, 2024, **128**, 2939–2947.
15 F. Castiglione, G. Raos, G. B. Appetecchi, M. Montanino, S. Passerini, M. Moreno, A. Famulari and A. Mele, *Phys. Chem. Chem. Phys.*, 2010, **12**, 1784–1792.
16 G. Annat, M. Forsyth and D. R. MacFarlane, *J. Phys. Chem. B*, 2012, **116**, 8251–8258.
17 M. T. Clough, C. R. Crick, J. Grasvik, P. A. Hunt, H. Niedermeyer, T. Welton and O. P. Whitaker, *Chem. Sci.*, 2015, **6**, 1101–1114.
18 M. Kunze, S. Jeong, G. B. Appetecchi, M. Schönhoff, M. Winter and S. Passerini, *Electrochim. Acta*, 2012, **82**, 69–74.
19 N. Abdou, A. Pipertzis, J. Swenson and A. Martinelli, *J. Mol. Liq.*, 2025, **437**, 128418–128427.
20 G. B. Appetecchi, M. Montanino, A. Balducci, S. F. Lux, M. Winterb and S. Passerini, *J. Power Sources*, 2009, **192**, 599–605.
21 Q. Zhou, W. A. Henderson, G. B. Appetecchi and S. Passerini, *J. Phys. Chem. C*, 2010, **114**, 6201–6204.
22 Q. Zhou, P. D. Boyle, L. Malpezzi, A. Mele, J.-H. Shin, S. Passerini and W. A. Henderson, *Chem. Mater.*, 2011, **23**, 4331–4337.
23 P. M. Bayley, A. S. Best, D. R. MacFarlane and M. Forsyth, *ChemPhysChem*, 2011, **12**, 823–827.
24 M. Nádherná, J. Reiter, J. Moškon and R. Dominko, *J. Power Sources*, 2011, **196**, 7700–7706.
25 A. Lahiri, T. J. Schubert, B. Iliev and F. Endres, *Phys. Chem. Chem. Phys.*, 2015, **17**, 11161–11164.
26 M. Holz and H. Weingartner, *J. Magn. Reson.*, 1991, **92**, 115–125.
27 M. Herstedt, M. Smirnov, P. Johansson, M. Chami, J. Grondin, L. Servant and J. C. Lassègues, *J. Raman Spectrosc.*, 2005, **36**, 762–770.
28 L. Li, S. Zhou, H. Han, H. Li, J. Nie, M. Armand, Z. Zhou and X. Huang, *J. Electrochem. Soc.*, 2011, **158**, A74–A82.
29 M. Kunze, S. Jeong, E. Paillard, M. Winter and S. Passerini, *J. Phys. Chem. C*, 2010, **114**, 12364–12369.
30 M. Kerner, N. Plylahan, J. Scheers and P. Johansson, *Phys. Chem. Chem. Phys.*, 2015, **17**, 19569–19581.
31 P. Gerlach, R. Burges, A. Lex-Balducci, U. S. Schubert and A. Balducci, *J. Electrochem. Soc.*, 2020, **167**, 120546.
32 C. A. Angell, N. Byrne and J.-P. Belieres, *Acc. Chem. Res.*, 2007, **40**, 1228–1236.
33 W. Xu, E. I. Cooper and C. A. Angell, *J. Phys. Chem. B*, 2003, **107**, 6170–6178.
34 K. Ueno, H. Tokuda and M. Watanabe, *Phys. Chem. Chem. Phys.*, 2010, **12**, 1649–1658.
35 H. Yoon, A. S. Best, M. Forsyth, D. R. MacFarlane and P. C. Howlett, *Phys. Chem. Chem. Phys.*, 2015, **17**, 4656–4663.
36 P. Sippel, P. Lunkenheimer, S. Krohns, E. Thoms and A. Loidl, *Sci. Rep.*, 2015, **5**, 13922–13929.
37 J. B. Haskins, W. R. Bennett, J. J. Wu, D. M. Hernández, O. Borodin, J. D. Monk, C. W. J. Bauschlicher and J. W. Lawson, *J. Phys. Chem. B*, 2014, **118**, 11295–11309.
38 F. Castiglione, E. Ragg, A. Mele, G. B. Appetecchi, M. Montanino and S. Passerini, *J. Phys. Chem. Lett.*, 2011, **2**, 153–157.
39 F. Lundin, A. Idström, P. Falus, L. Evenäs, S. Xiong and A. Matic, *J. Phys. Chem. C*, 2022, **126**, 16262–16271.

40 F. Castiglione, M. Moreno, G. Raos, A. Famulari, A. Mele, G. B. Appetecchi and S. Passerini, *J. Phys. Chem. B*, 2009, **113**, 10750–10759.

41 M. Gouverneur, J. Kopp, L. van Wullen and M. Schonhoff, *Phys. Chem. Chem. Phys.*, 2015, **17**, 30680–30686.

42 O. Holloczki, F. Malberg, T. Welton and B. Kirchner, *Phys. Chem. Chem. Phys.*, 2014, **16**, 16880–16890.

43 K. Ueno, H. Tokuda and M. Watanabe, *Phys. Chem. Chem. Phys.*, 2010, **12**, 1649–1658.

44 I. Rey, P. Johansson, J. Lindgren, J. C. Lassègues, J. Grondin and L. Servant, *J. Phys. Chem. A*, 1998, **102**, 3249–3258.

45 J. C. Lassègues, J. Grondin, R. Holomb and P. Johansson, *J. Raman Spectrosc.*, 2007, **38**, 551–558.

46 S. Duluard, J. Grondin, J.-L. Bruneel, I. Pianet, A. Grélard, G. Campet, M.-H. Delville and J.-C. Lassègues, *J. Raman Spectrosc.*, 2008, **39**, 627–632.

47 J.-C. Lassègues, J. Grondin, C. Aupetit and P. Johansson, *J. Phys. Chem. A*, 2009, **113**, 305–314.

48 J. Pitawala, A. Martinelli, P. Johansson, P. Jacobsson and A. Matic, *J. Non-Cryst. Solids*, 2015, **407**, 318–323.

49 K. Fujii, S. Seki, S. Fukuda, R. Kanzaki, T. Takamuku, Y. Umebayashi and S.-I. Ishiguro, *J. Phys. Chem. B*, 2007, **111**, 12829–12833.

50 K. Fujii, H. Hamano, H. Doi, X. Song, S. Tsuzuki, K. Hayamizu, S. Seki, Y. Kameda, K. Dokko, M. Watanabe and Y. Umebayashi, *J. Phys. Chem. C*, 2013, **117**, 19314–19324.